Hindawi
Structural Control and Health Monitoring
Volume 2023, Article ID 2568963, 22 pages
https://doi.org/10.1155/2023/2568963

Research Article

Dynamic Characteristics of a Novel Right-Angle Viscoelastic Damper (RVD) Using Polyurethane Damping Materials

Jun-Hong Xu,[1] **Zhe-Yu Zhu**,[1] **Guang-Dong Zhou**,[2] **Hao Wang**,[3] **and Ai-Qun Li**[3,4]

[1]*School of Civil Engineering, Nanjing Forestry University, Nanjing, China*
[2]*School of Civil and Traffic Engineering, Hohai University, Nanjing, China*
[3]*School of Civil Engineering, Southeast University, Nanjing, China*
[4]*School of Civil and Traffic Engineering, Beijing University of Civil Engineering and Architecture, Beijing, China*

Correspondence should be addressed to Jun-Hong Xu; xujunhong0321@126.com

Received 12 September 2022; Revised 24 November 2022; Accepted 26 November 2022; Published 8 February 2023

Academic Editor: Zoran Rakicevic

Excessive plastic deformation may occur at the beam-column joints under seismic action and lead to connection failure, increasing the possibility of collapse of the entire frame structure. In order to improve the seismic performance of assembled steel structure joints, a right-angle viscoelastic joint damper with polyurethane as the core energy dissipation material is proposed in this paper. First, the temperature scanning tests of polyurethane materials were carried out based on the dynamic mechanical analysis method. Second, the dynamic mechanical test and numerical simulation analysis of the designed right-angle viscoelastic damper were performed to reveal the dynamic energy dissipation characteristics of the right-angle damper. Finally, the dynamic time-history damping analysis was performed on the steel frame structure equipped with RVDs. The results show that the TA value of polyurethane material reached its peak at 2.0 Hz, which is the ideal frequency for the material's damping ability. The right-angle damper made of polyurethane material has a softening nonlinear characteristic, and the peak value of the loss factor was obtained at 2.0 Hz, which is consistent with the results of the dynamic performance of the polyurethane material. The numerical simulation results demonstrate that stress on the steel plates and viscoelastic layers is reasonable. When the excitation level did not exceed 9 mm displacement amplitude, the energy input to the damper was dissipated by polyurethane, and the steel plates never showed plastic deformation. The time-history analysis of the steel structure shows that the dampers designed in this paper have a good control effect on the interstory displacement, acceleration, and interstory shear force of the structure. The research results lay the necessary foundation for the engineering application of polyurethane materials in the field of beam-column joints vibration damping.

1. Introduction

The assembled steel structure has greater advantages in development and good application prospects, but its beam-column joints have suffered significant damage in successive earthquakes [1, 2]. The mechanical properties of the beam-column joints play a crucial role in the safety and integrity of the entire frame system [3–7]. Based on the concept of passive control, the method of setting viscoelastic dampers at beam-column joints can provide additional stiffness and additional damping to the structure. The joint damper can assist the structure in forming an acceptable form of "strong joints and weak components" to better safeguard the global stability of the frame structure under earthquake action [8, 9]. In addition to ground motion, viscoelastic dampers also have excellent control effects on wind-induced vibration [10]. The passive damper also has a positive impact on the resilience of the building [11, 12].

The joint dampers include metal joint dampers and sector lead viscoelastic dampers, among which the sector lead viscoelastic dampers have been studied more. Wu et al. [13] designed and fabricated the sector lead viscoelastic damper (SLVD) and found that the shear modulus of the rubber and the strain amplitude had some influence on the SLVD performance. With the increase of the strain amplitude, the energy dissipation coefficient and the equivalent

viscous damping ratio increased and then decreased; with the increase of rubber's shear modulus, the initial stiffness, postyield stiffness, and equivalent stiffness increased, but the energy dissipation coefficient and equivalent viscous damping ratio decreased, and the loading frequency had a small effect on the performance of this damper. Wu et al. [14, 15] studied the performance of a seismic device with the joint SLVD and analyzed the effects of different strain amplitudes, loading frequencies, and shear modulus of the rubber on the performance of the damper. Zhu et al. [16] designed and analyzed the frame structure equipped with the SLVD from the view of stiffness, and the theoretical method for the design of dampers was given. Xu et al. [17] investigated the effect of the number and diameter of lead cores on the performance of the SLVD, and the results showed that the energy dissipation coefficient and equivalent damping ratio of the dampers increased with the increase of the number and diameter of lead cores. But Zhang et al. [18] conducted a destructive damaged retrofitting study on an RC frame equipped with the SLVD and found that the thickness of viscoelastic materials and the diameter of lead cores contributed less to the improvement of seismic performance, while the effective radius of the sector provided a larger contribution.

According to the aforementioned studies, the beam-column joints of the joint viscoelastic damper have a problem with small corner deformation [19]. Additionally, during the manufacturing process, the shape of the damper is curved, and there are numerous mold parts for making components, up to 20 different types [20]. In order to fully utilizing the energy dissipation capability of the damper, this paper proposes the right-angle viscoelastic damper, which has a relatively simple structure (the structural layout is shown in Figure 1). As can be seen from the figure, the damper is bolted to the armpit of the beam and column, which not only has the advantages of small size and does not affect the use of space but also can play a role in fixing the frame beam when installing the assembled beam structure.

The vibration reduction mechanism of the damper is that under the horizontal action of the earthquake, the bending deformation of the beam at the joint causes the rotation of the frame beam-column joint, and the rotation can cause the steel plates of the damper connected to the beam and column, respectively, to rotate and displace, which drives the material layers of the right-angle damper to shear deformation to achieve energy dissipation. When damage occurs to the damper, the overall damage to the structure does not develop excessively, although the function of the damper will be affected or even destroyed to some extent. The expected function of the structure can still be restored after the repair under reasonable technical and economic conditions.

As a typical representative of polymer products, polyurethane has characteristics that fall in between those of rubber and plastic. Its intermolecular force is strong, and the biggest characteristic of polyurethane is that it still maintains elasticity under high hardness, coupled with good abrasion resistance, oil resistance, low-temperature resistance, ozone aging resistance, and other properties. Therefore, the material has a wide range of applied research in the field of

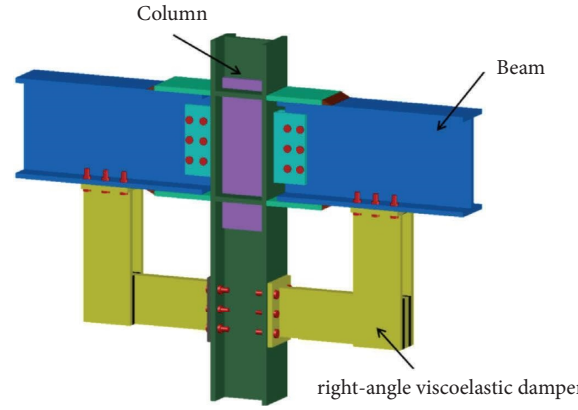

Figure 1: Layout of the right-angle viscoelastic damper (yellow part) at beam-column joints.

damping materials [21, 22]. From the microscopic point of view, polyurethane has good damping and mechanical properties, [23] which is related to its main chain containing both soft and hard segments. The two segments determine different properties. The soft and hard segments produce different movement responses to external forces, which can cause interfacial frictions, resulting in energy consumption [24].

Therefore, a right-angle viscoelastic joint damper with polyurethane as the core energy-dissipating material was designed in this paper. First, temperature scanning performance tests were conducted on polyurethane materials to derive the variation patterns of loss factor, shear modulus, and loss modulus with the temperature at different frequencies of the materials. Second, dynamic performance tests were carried out on right-angle viscoelastic dampers to investigate the displacement dependence and frequency dependence of the dynamic mechanical performance parameters of the dampers. Furthermore, the experimental results of the damper were verified by numerical simulation, and the distribution of stress and energy dissipation conditions of the damper was discussed. Finally, for one steel frame damping structure, the comparative seismic response analysis was conducted to explore the damping effect of the RVD damping system.

2. Dynamic Thermodynamic Testing of Polyurethane Rubber

In order to improve the accuracy of the temperature dependence, DMA tests were first conducted on the polyurethane material used in the damper. The tests were performed with a dynamic thermomechanical analyzer of type DMA 242E from NETZSCH, Germany. Cut the vulcanized polyurethane rubber into rectangular sample strips measuring 50.0 mm × 11.0 mm × 2.5 mm. The specific test conditions were as follows: amplitude of 10 μm, temperature scanning range of −40 to 60°C, and the heating rate of 5°C/min. Corresponding to the damper tests, a total of four test frequencies of 0.5, 1.0, 1.5, and 2.0 Hz were set.

The curves of storage modulus E', loss modulus E'', and loss factor tan δ versus time for polyurethane materials are shown in Figure 2. Figures 2(a)–2(d) represent the curves at 0.5, 1.0, 1.5, and 2.0 Hz, respectively. It can be seen from the figure that the performance of polyurethane materials is stable, and its loss modulus and loss factor both tend to increase and then decrease with the increase in temperature, while the storage modulus gradually decreases with the increase in temperature. The loss factor achieves a maximum value of 0.62 at 0.5 Hz operating conditions.

The most scientific method to characterize the damping performance of the material is to use the value of the integrated area of the material loss factor curve over temperature tanδ area, namely TA value, as the damping evaluation index. The formula of calculation is shown as follows [25]:

$$\mathrm{TA} = \int_{T_G}^{T_R} \tan\delta \, dT \cong \left(\ln E'_G - \ln E'_R\right) \frac{R}{(E_a)_{\mathrm{avg}}} \frac{\pi}{2} T_g^2, \quad (1)$$

where E'_G and E'_R refer to the loss modulus value of the glassy state and the loss modulus value of the rubber state, respectively; T_G and T_R refer to the minimum value of the glass transition temperature and the maximum value of the rubber state transition temperature, respectively; R refers to polymer gas constant; $(E_a)_{\mathrm{avg}}$ refers to average activation energy during relaxation.

The curves of the damping performance parameters of the polyurethane material with the loading frequency are given in Figures 3(a) and 3(b), including the TA value, the peak loss factor ($\tan\delta_{\max}$), the wide damping temperature range (i.e., the temperature interval $\Delta T_{0.5}$ where the loss factor is greater than 0.5), and the temperature of glass transition peak T_g. As can be seen from the figure, $\Delta T_{0.5}$ decreases first and then increases with the increase of frequency and reaches its maximum value at 0.5 Hz while the temperature of glass transition peak T_g increases and then decreases with the increase of frequency. The TA value increases gradually with the increase of frequency and reaches the maximum value of 28.2°C when the loading frequency is 2.0 Hz, which is the best frequency to play the damping performance in the material tests. The variation trend of the material damping properties with temperature can be clearly derived from the temperature scanning curve.

3. Testing of Polyurethane Right-Angle Viscoelastic Dampers

3.1. Design and Loading Scheme of the Right-Angle Viscoelastic Damper (RVD) Specimens. The right-angle viscoelastic damper specimens designed in this paper, which has a steel plate for shearing at right angles to the steel plates for constraint, are conveniently arranged at the beam-column joints. The size of the plate for constraint is 150 mm × 100 mm × 12 mm, and the size of the plate for shearing is 150 mm × 100 mm × 20 mm. The viscoelastic material is made of polyurethane rubber with two layers, each of which is 100 mm × 100 mm × 6 mm in size. The specific construction is shown in Figure 4(a).

Due to the structural peculiarity that the loading end and fixed end of the designed damper are not in the same straight line, the loading device requires a special design. The loader is a servo actuator (MTS) with a loading capacity of 1000 kN. A right-angle steel plate was placed on the test bench, and it was fixed to the test bench by bolts. The fixed end of the RVD was fastened on the vertical surface of the right-angle steel plate by the steel plate for connection, and the shear end was connected to the MTS machine by a steel rod. The three-dimensional view of the loading device, the actual damper, and the view of the actual loading device are shown in Figures 4(b)–4(d), respectively.

As listed in Table 1, there are sixteen loading conditions in total. Five laps were loaded for each working condition, and the hysteresis curve of the third lap was taken as the calculated mechanical property index curve.

3.2. Force-Displacement Hysteresis Curves of the Right-Angle Damper. The damper test was conducted at room temperature (the field measurement temperature was 21°C), and the hysteresis curves obtained according to the loading scheme in Table 2 are shown in Figure 5. Figures 5(a)–5(d) show the force-displacement hysteresis curves at frequencies of 0.5, 1.0, 1.5, and 2.0 Hz for displacement amplitudes of 1.2, 3, 6, and 9 mm, respectively. It can be seen that the hysteresis curves for all displacement conditions are elliptical, smooth, and relatively full, characterized by the fact that the maximum damping force and the maximum deformation do not occur simultaneously due to the viscous resistance of the right-angle damper, and there is a certain phase difference. The shape of the hysteresis loop varies with the displacement amplitude, and the hysteresis characteristics of the right-angle damper show nonlinear feature at this time. The slope of the hysteresis curves decreases with the increase of the displacement amplitude for all frequency conditions, indicating that the stiffness of the damper also tends to decrease with increasing displacement amplitude. In summary, it can be seen that the right-angle damper made of polyurethane materials has softening nonlinear characteristics.

3.3. Frequency Dependence of Hysteresis Curves. Figures 6(a)–6(d) show the frequency dependence of hysteresis curves for the four displacement conditions (1.2 mm, 3 mm, 6 mm, and 9 mm), respectively. As can be seen from the figure, when the displacement amplitude is 1.2 and 3 mm, the slope of the hysteresis curve shows an increasing trend with the increase of frequency, while the slope of the 3 mm displacement amplitude working condition has a smaller increase with the increase of frequency. The four frequency curves overlap with similar slopes at the 6 mm displacement amplitude working condition. At the 9 mm displacement condition, the slope of the curve tends to decrease as the frequency increases. The frequency dependence analysis under the four displacement conditions shows that the slope of the curve tends to increase from upward to downward as the displacement increases. The frequency dependence is most obvious at 1.2 mm displacement amplitude working condition and least obvious at 6 mm.

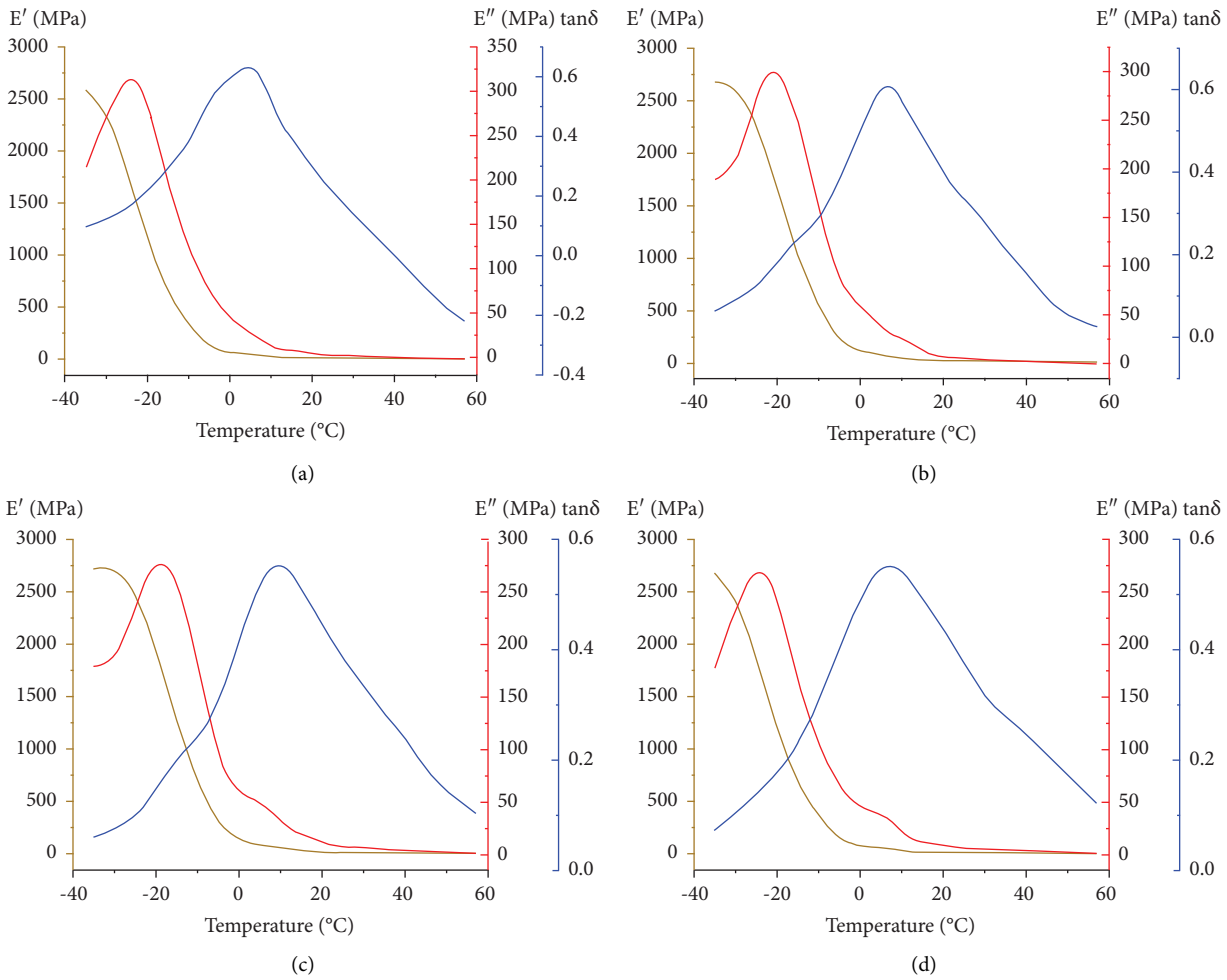

Figure 2: E'' -T, E' -T, tan δ-T curves of polyurethane rubber: (a) 0.5 Hz; (b) 1.0 Hz; (c) 1.5 Hz; (d) 2.0 Hz.

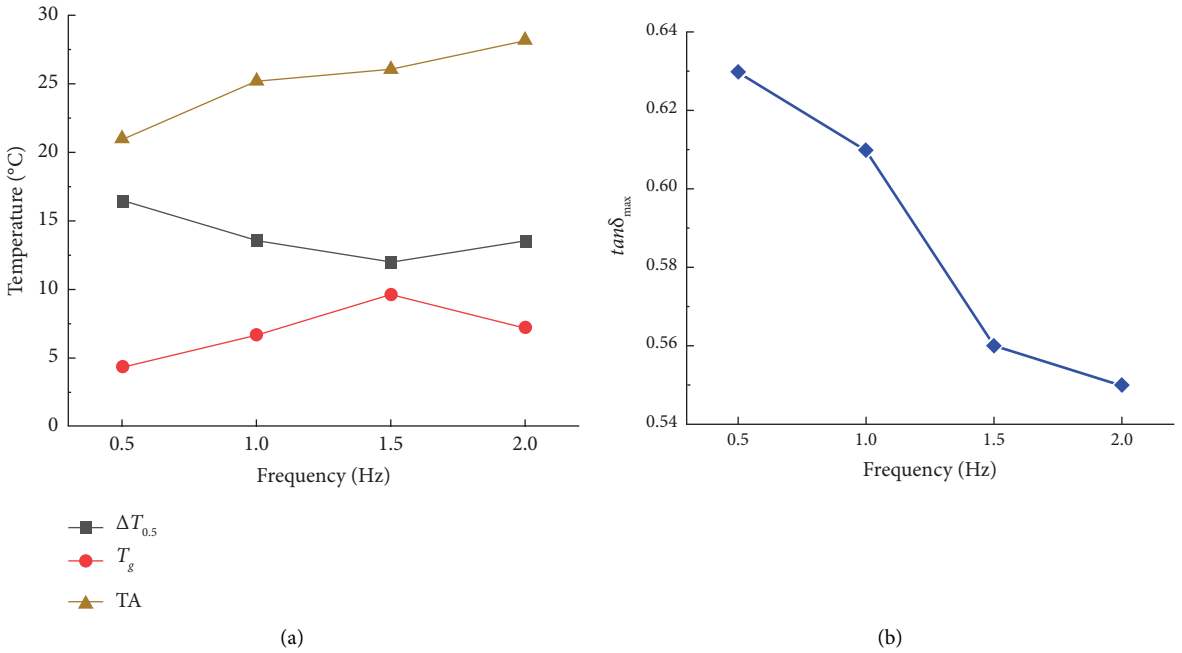

Figure 3: Parameters' value of polyurethane rubber at different frequencies: (a) $\Delta\ (T)_{0.5}$, T_g and TA; (b) $\tan\delta_{max}$.

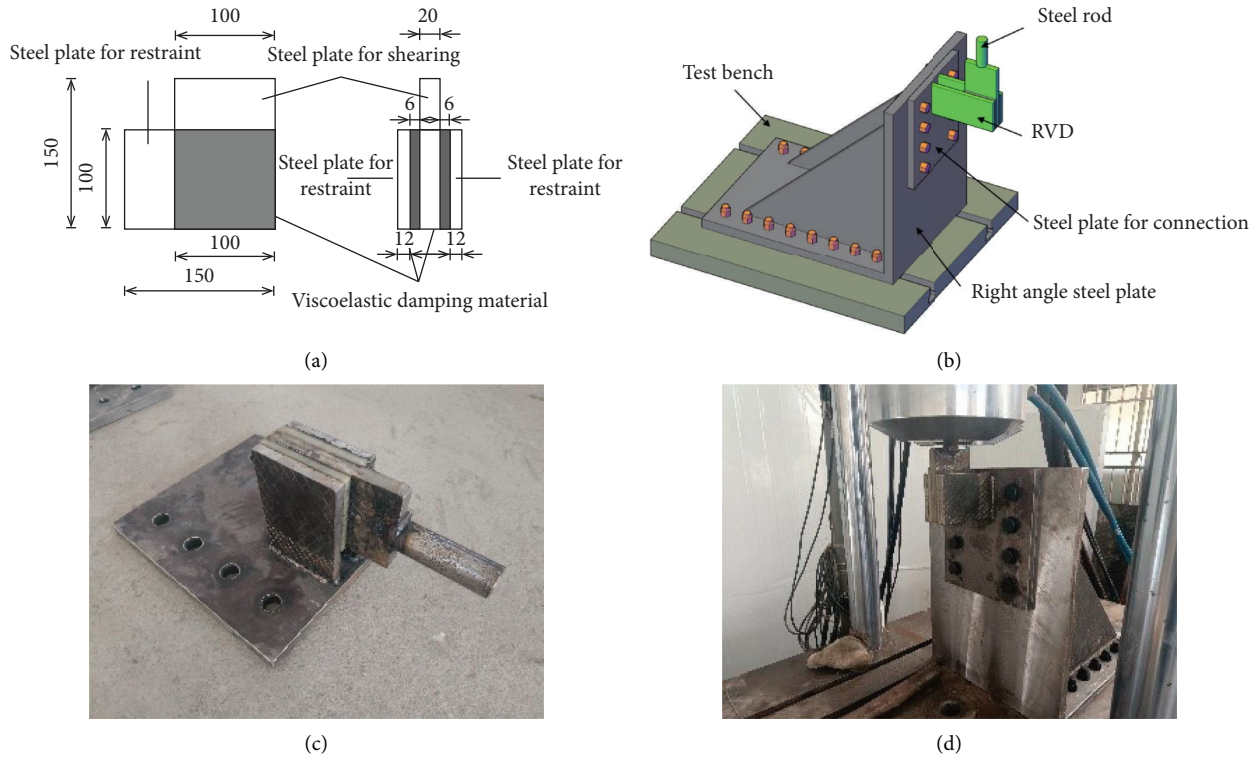

Figure 4: Experimental diagram: (a) geometric dimension of RVD (unit : mm); (b) three-dimensional view of loading device; (c) actual RVD; (d) view of the actual loading device.

Table 1: Test schemes of the viscoelastic damper.

Experimental conditions	Displacement amplitude (mm)	Loading frequency (Hz)	Number of cycles (times)
TEST-1	1.2 (20%)	0.5/1/1.5/2	5
TEST-2	3 (50%)	0.5/1/1.5/2	5
TEST-3	6 (100%)	0.5/1/1.5/2	5
TEST-4	9 (150%)	0.5/1/1.5/2	5

Table 2: Plastic parameters of steel.

i	Yield stress (MPa)	Plastic strain
1	232.18	0
2	249.94	0.0683
3	263.45	0.0843
4	298.56	0.1134
5	315.4	0.1437
6	336.44	0.1925

4. Analysis of Dynamic Characteristic Index

A series of mechanical parameters of right-angle dampers were calculated from the hysteresis curve sets derived from the tests.

4.1. Maximum Damping Force F_{max}. Figure 7 shows the displacement and frequency dependence analysis of $F_{\max}$. From Figure 7(a), it can be seen that $F_{\max}$ shows a trend of increasing and then decreasing with the increase of displacement at all four frequencies. $F_{\max}$ for all frequencies except 0.5 Hz reaches its maximum value at 6 mm displacement. From Figure 7(b), it can be seen that $F_{\max}$ increases with increasing frequency at the displacement amplitudes of 1.2 and 3 mm, while at 9 mm displacement, $F_{\max}$ decreases with the increase of frequency. The trend of $F_{\max}$ variation is not significant at the displacement amplitude of 6 mm. The maximum value of 14.1 kN is obtained at 6 mm displacement amplitude and 1.0 Hz frequency in all operating conditions.

4.2. Storage Stiffness K' d. The storage stiffness is related to the ability of the damper in terms of energy conversion, and the displacement dependence and frequency dependence of

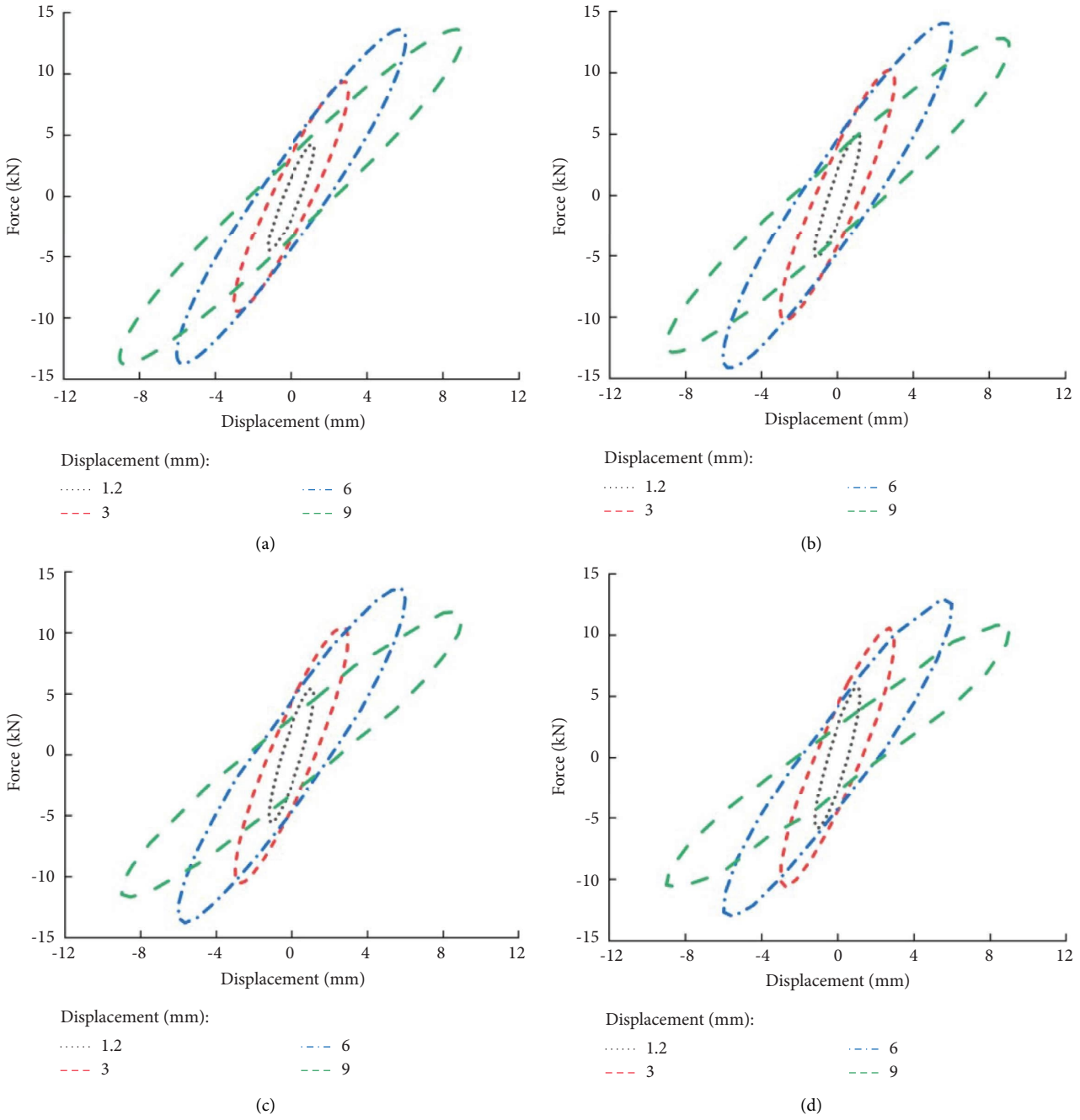

Figure 5: Hysteretic curves of RVD at different frequencies and displacements: (a) 0.5 Hz; (b) 1.0 Hz; (c) 1.5 Hz; (d) 2.0 Hz.

the storage stiffness are shown in Figure 8. Figure 8(a) shows that the storage stiffness tends to decrease with the increase of displacement amplitude at all frequencies, and the four curves vary more closely. The value of maximum stored stiffness is obtained at the displacement amplitude of 1.2 mm and loading frequency of 1.5 Hz, which is 4.2 kN/mm. From the diagrams of frequency dependence shown in Figure 8(b), it can be seen that the other four variation curves are approximately horizontal except for the larger rise at the displacement of 1.2 mm.

4.3. Loss Stiffness K'' d. The loss stiffness K'' d reflects the energy loss performance of the damper, and its dependence analysis graph is shown in Figure 9. From the displacement dependence analysis graph in Figure 9(a), it can be seen that the variation law of the displacement dependence is similar to the law of the storage stiffness, which has the overall monotonic decreasing variation. The maximum value is obtained at the displacement amplitude of 1.2 mm and loading frequency of 2.0 Hz, which is 2.2 kN/mm. From Figure 9(b), it can be seen that K'' d increases with increasing

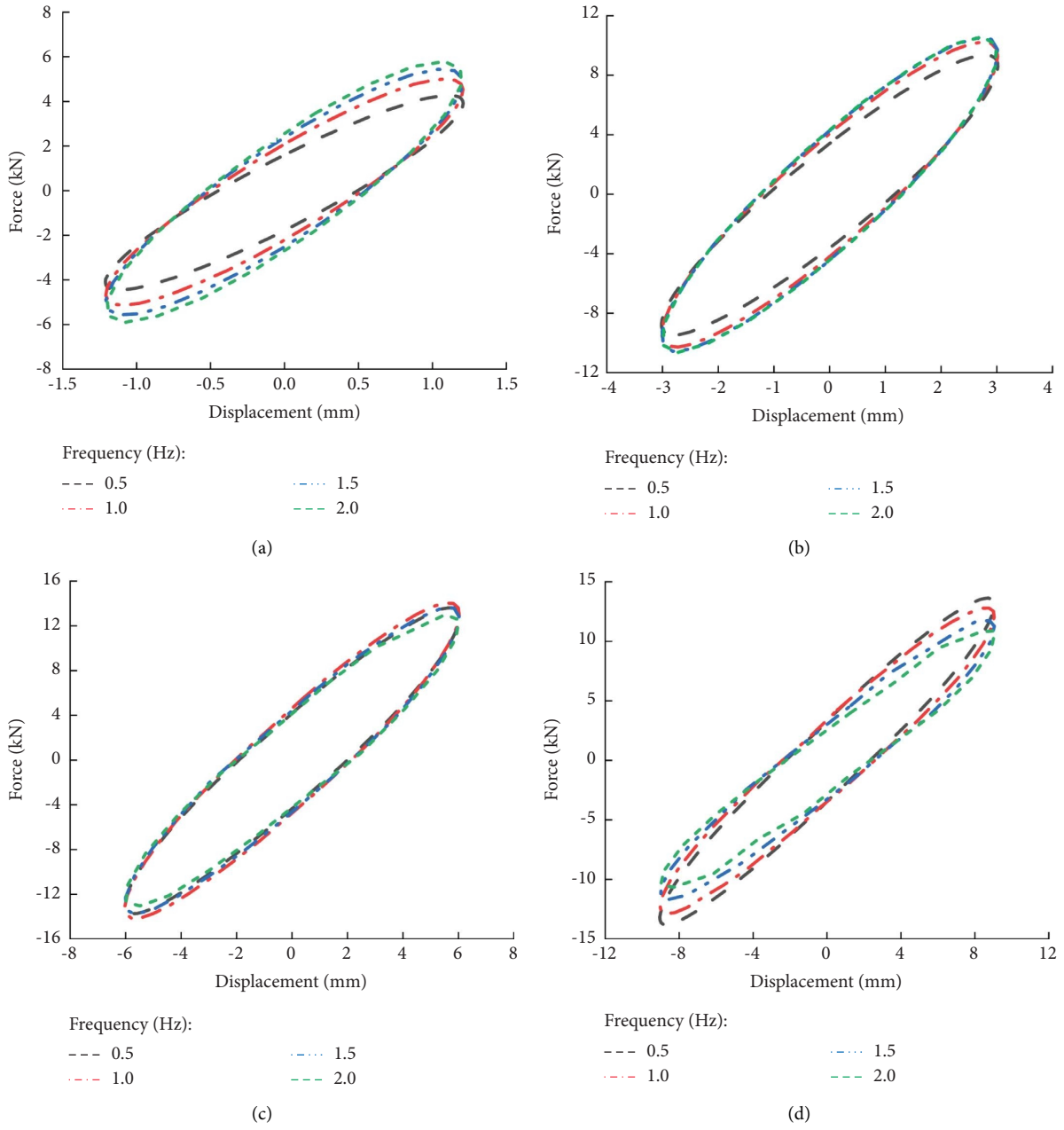

Figure 6: Frequency dependence of hysteretic curves: (a) 1.2 mm; (b) 3 mm; (c) 6 mm; (d) 9 mm.

frequency for displacement amplitudes of 1.2 and 3 mm. The curves of 6 mm and 9 mm are flatter, with a slight drop and less variation.

4.4. Equivalent Damping Coefficient C_d. The equivalent damping coefficient is a parameter that reflects the value of the basic mechanical properties of the damper. As shown in the displacement dependence diagrams of the equivalent damping coefficient in Figure 10(a), the four curves show an overall monotonically decreasing trend with the increase of displacement, which is consistent with the variation law of the loss factor derived from the temperature scanning test of energy-consuming materials polyurethane. With the increase in frequency, the curves decrease slowly, and the maximum value of C_d is 3.0 N s/mm at the displacement amplitude of 1.2 mm and the loading frequency of 0.5 Hz. Comparing Figures 10(a) and 10(b), it can be seen that the displacement dependence and frequency dependence have similar trends. The equivalent damping coefficient at each displacement shows a monotonically decreasing trend with the increase of frequency, and the decreasing trend becomes slower with increasing displacement amplitude, and the value of C_d at the same frequency also decreases gradually.

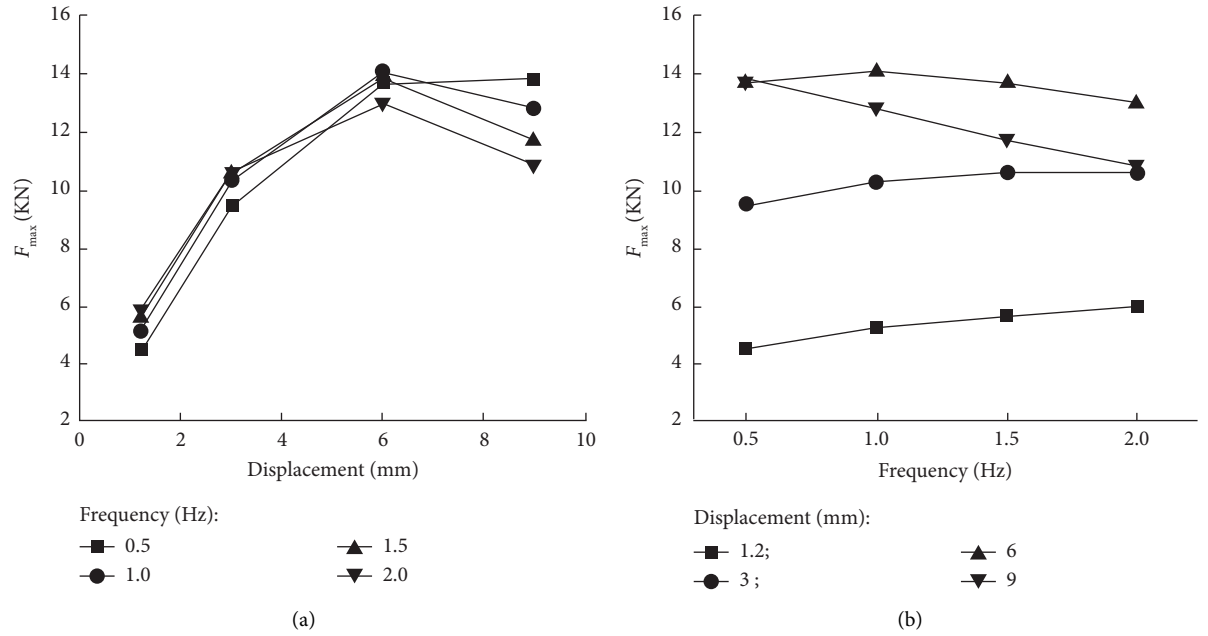

Figure 7: Maximum damping force dependence analysis diagrams: (a) displacement dependence; (b) frequency dependence.

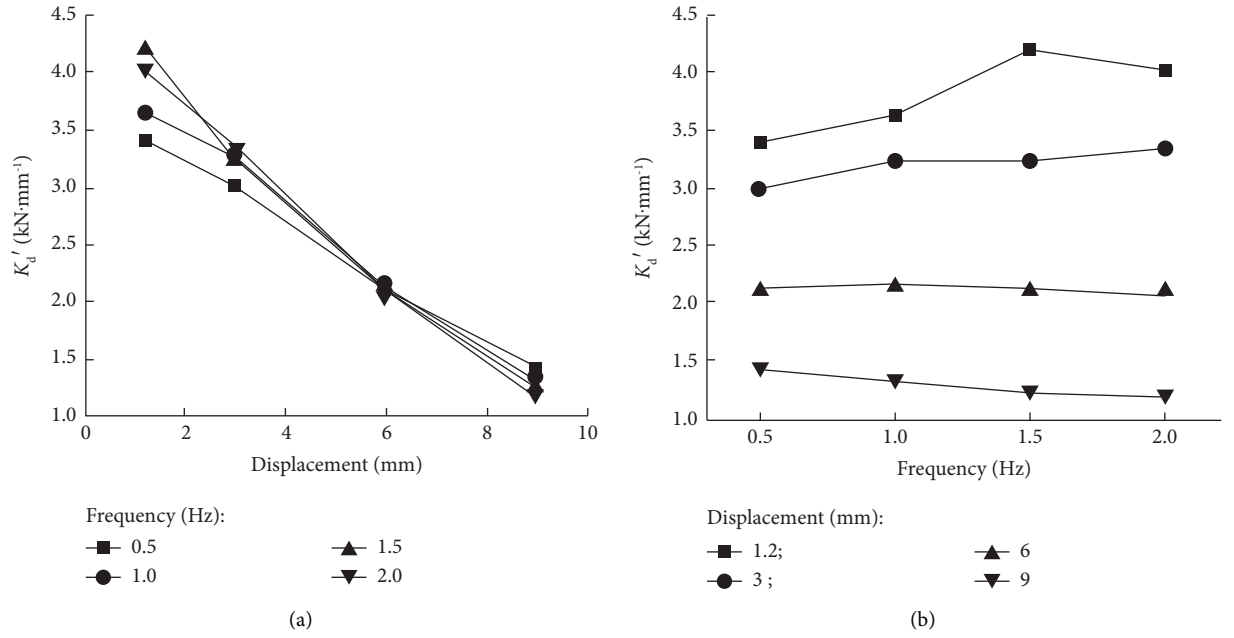

Figure 8: Storage stiffness dependence analysis diagrams: (a) displacement dependence; (b) frequency dependence.

4.5. Shear Modulus $\boldsymbol{G'}$ and $\boldsymbol{G''}$. The shear modulus includes shear storage modulus and shear loss modulus, which are related to the storage and loss stiffnesses as well as the thickness and shear area of viscoelastic materials, so their variation laws are highly similar to the storage and loss stiffnesses, respectively.

For the shear storage modulus G', as shown in Figure 11(a), the curves are monotonically decreasing with increasing displacement, and the maximum value of 1.3 MPa is obtained at the displacement of 1.2 mm and the frequency of 1.5 Hz. The frequency dependence of the shear storage modulus as shown in Figure 11(b) changes in the same way as the storage stiffness. For the shear loss modulus G'', as shown in Figures 12(a) and 12(b), the variation laws of the displacement-dependence and frequency-dependence curves are the same as the loss stiffness, and the maximum value of 0.7 MPa is obtained at the displacement of 1.2 mm and the frequency of 2.0 Hz.

4.6. Loss Factor η. The loss factor is an important parameter indicating the energy dissipation capacity of the damper, and the loss factor η dependence analysis diagrams are shown in

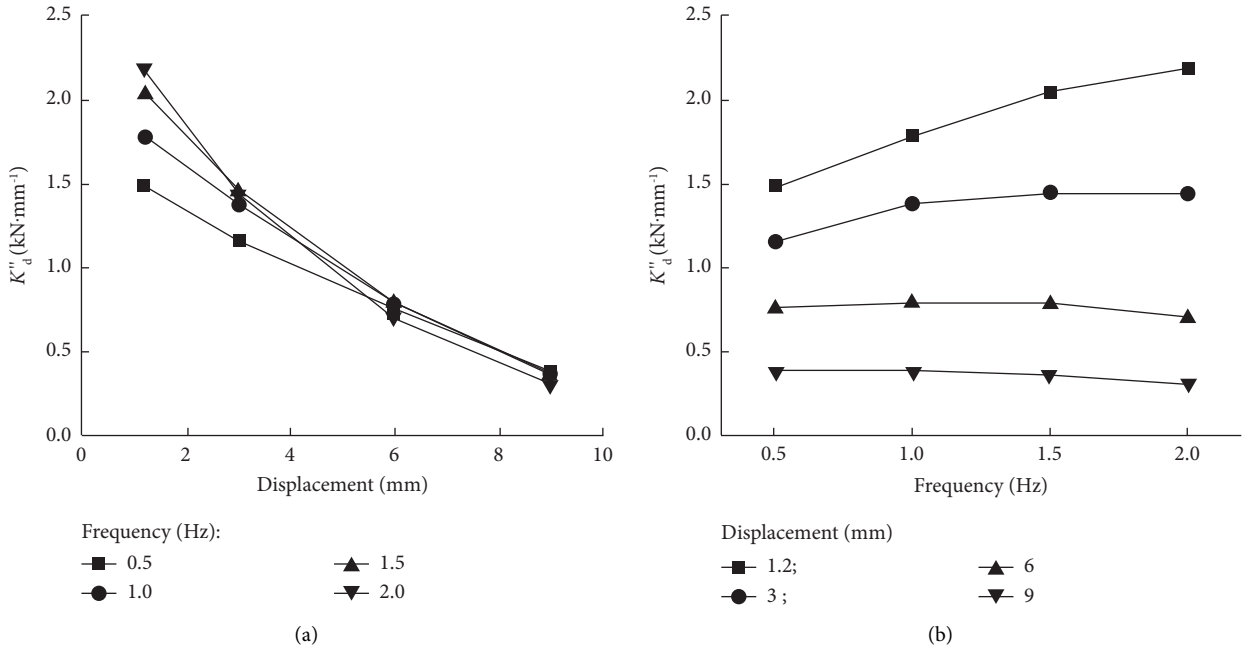

Figure 9: Loss stiffness dependence analysis diagrams: (a) displacement dependence; (b) frequency dependence.

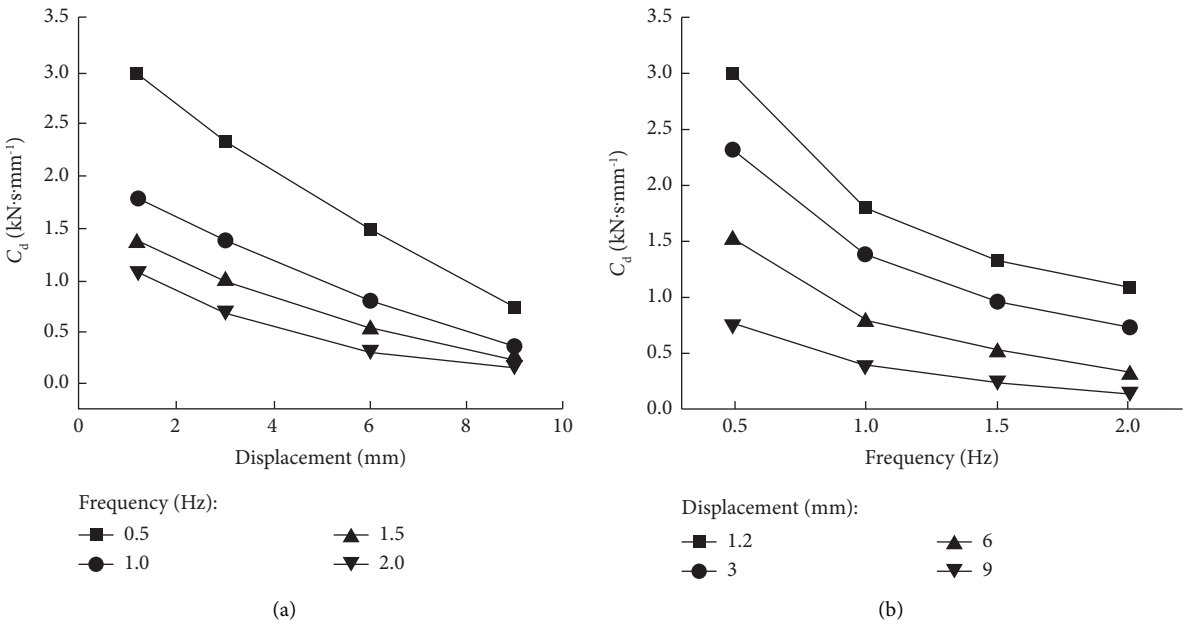

Figure 10: Equivalent damping coefficient dependence analysis diagrams: (a) displacement dependence; (b) frequency dependence.

Figures 13(a) and 13(b). From Figure 13(a), all curves decrease with the increase of displacement amplitude. The maximum loss factor is 0.55 when the frequency is 2.0 Hz, and the displacement amplitude is 1.2 mm.

5. Numerical Analysis with ABAQUS

In order to investigate the stress and energy dissipation mechanism inside the right-angle type damper steel plate and polyurethane, the ABAQUS refined finite element numerical analysis of the test damper was carried out in this thesis.

5.1. Geometric Modeling and Meshing. The steel plate and damping material of the damper were meshed, respectively. Figure 14(a) shows the model geometry of the damper. As shown in Figure 14(b), the approximate global sizes are 4 mm and 5 mm for the restrained and shear steel plates, respectively, and the approximate global size for the rubber is 2 mm. In order to make the calculation results more accurate and reasonable, the steel plate adopted the C3D8R meshing element type, and the damping material adopted the C3D8H meshing element type.

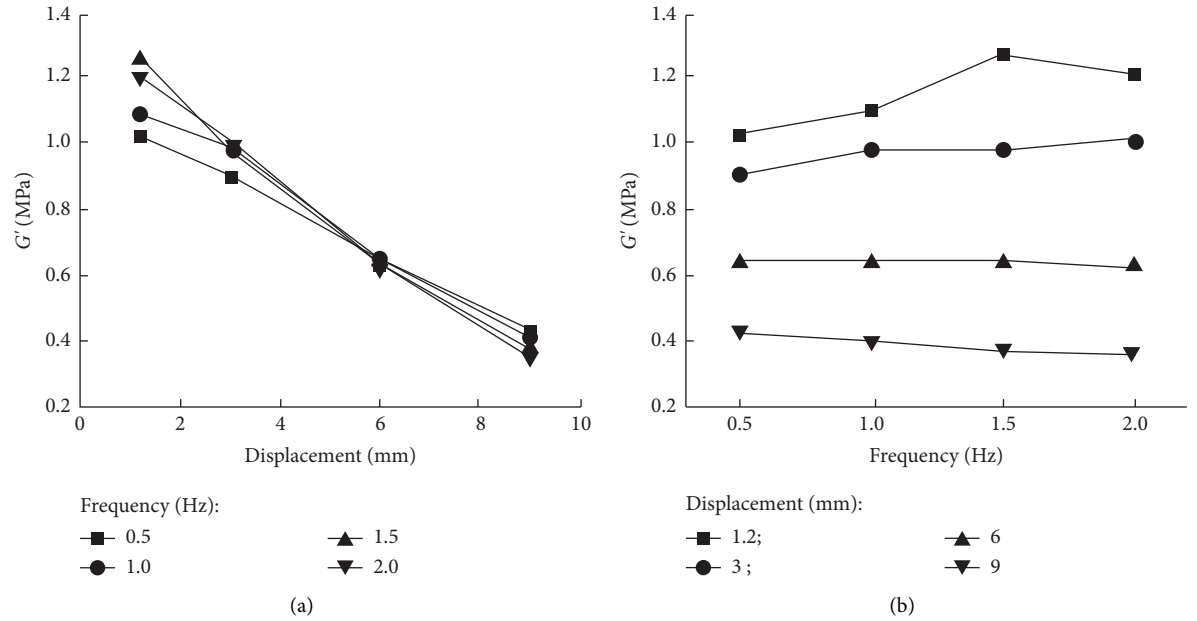

Figure 11: Storage modulus dependence analysis diagrams: (a) displacement dependence; (b) frequency dependence.

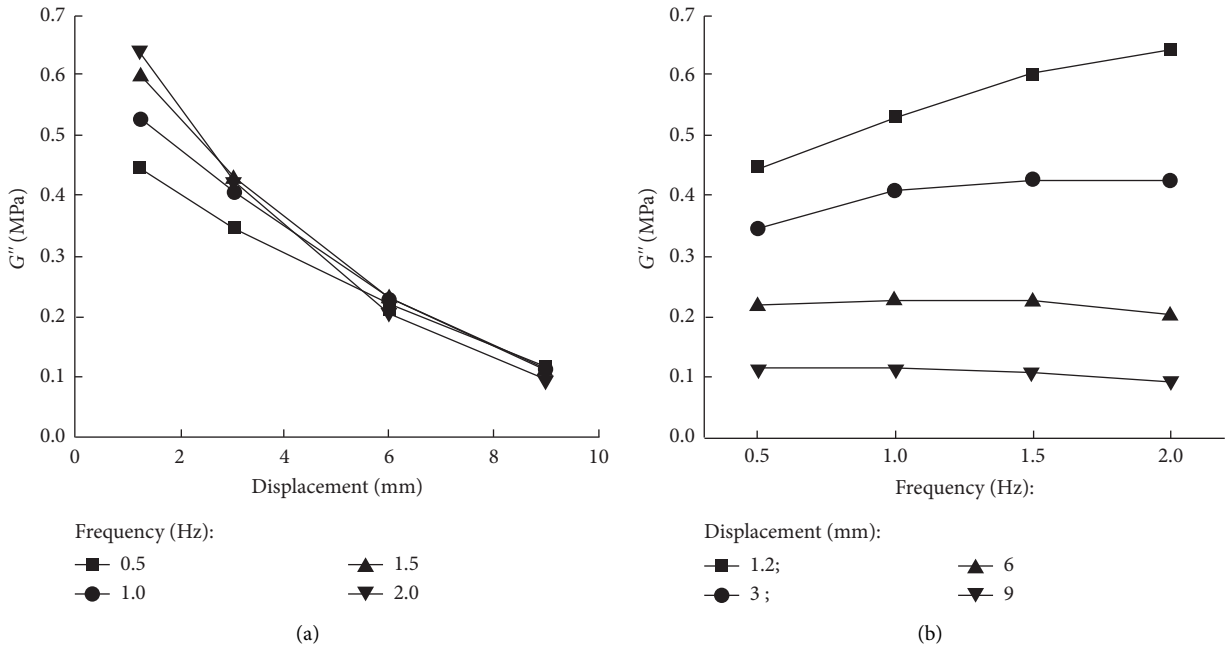

Figure 12: Loss modulus dependence analysis diagrams: (a) displacement dependence; (b) frequency dependence.

5.2. Properties of the Materials. The numerical simulation not only studies the change of energy dissipation of the damper but also explores whether plastic energy dissipation occurs in the steel plate, so the plastic characteristics are still defined on the basis of the defined elastic parameters. The Young's modulus and Poisson's ratio of steel plates were taken as 2.06×10^5 MPa and 0.3, respectively. The plastic parameters were defined in ABAQUS in terms of yield stress and plastic strain, as listed in Table 2, where i refers to the ith set of data that respond to the constitutive relation of the material.

For polyurethane materials, it was defined by two parameters, which are hyperelasticity and viscoelasticity. Hyperelasticity can be derived by fitting data obtained from uniaxial tensile tests, while viscoelastic parameters can be obtained by fitting data obtained from relaxation tests. Theoretically, Mooney-Rivlin is more suitable for strain values of 20% to 150% [26]. The maximum strain amplitude in this study is 150%, which all lies in the above interval, so the hyperelastic parameters can be simulated by Mooney-Rivlin. The specific parameters of hyperelasticity are listed in Table 3. As for viscoelasticity, the

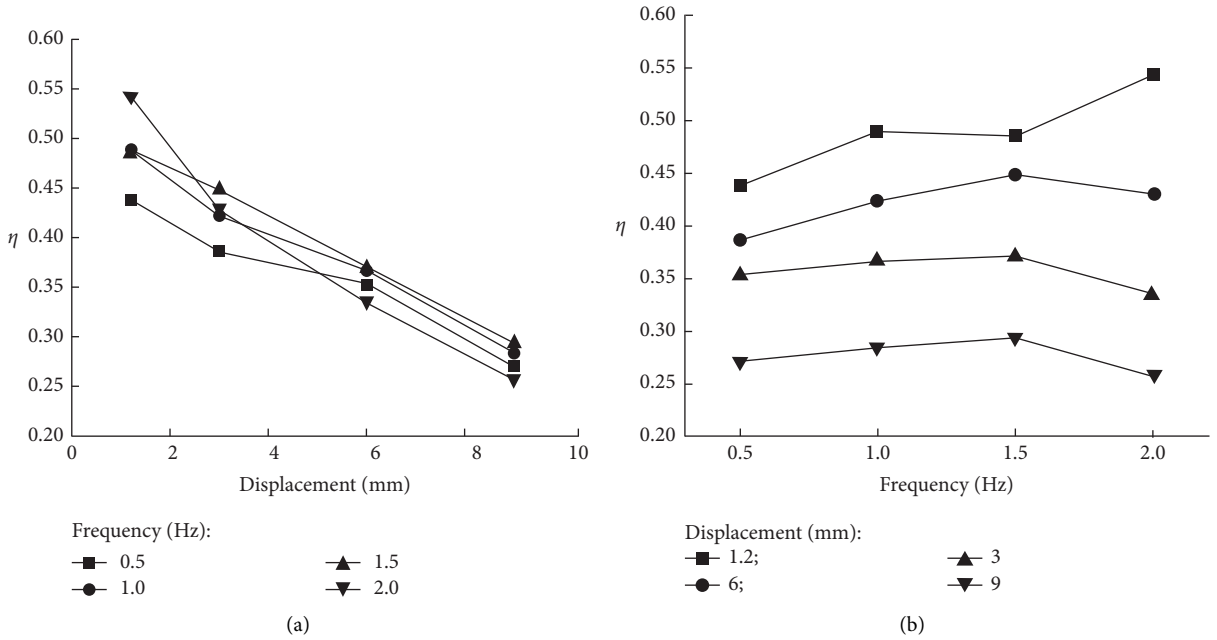

Figure 13: Loss factor dependence analysis diagrams: (a) displacement dependence; (b) frequency dependence.

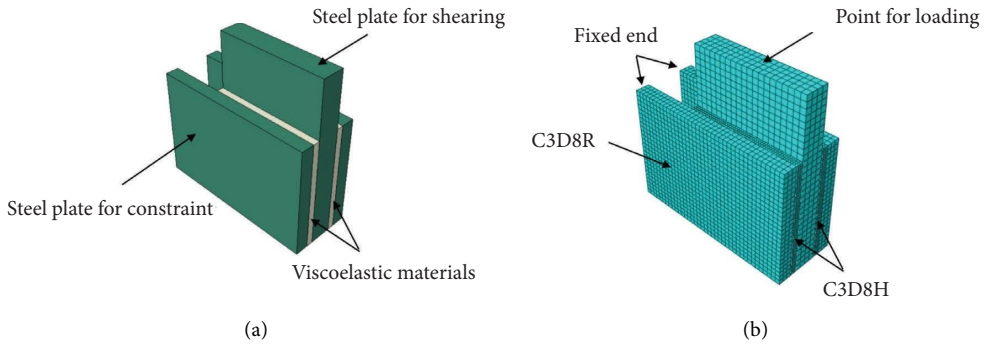

Figure 14: Numerical modeling: (a) model geometry; (b) model meshing.

Table 3: Hyperelastic parameters of rubber.

i	$C10$	$C01$	$D1$
1	0.129	0.00691	0

Prony sequence was used to simulate the time dependence of the rubber material, and the parameters used in this simulation are listed in Table 4.

5.3. Interaction and Boundary Conditions. The right-angle dampers in this study interacted in two places in ABAQUS. For one thing, in practice, the vulcanization bond between the viscoelastic material and the steel plate has strong integrity, so the viscoelastic layer was connected to the steel plate by tie binding in the simulation. For another thing, in the test, the upper part of the damper was connected to the MTS machine through a steel rod, and then, the displacement was applied. Therefore, a point was coupled in the center of the top surface of the shear steel plate in the simulation in order to apply the displacement condition there.

Table 4: Viscoelastic parameters of rubber.

i	g_i-prony	k_i-prony	τ_i-prony
1	0.4323	0	7.425×10^{-7}
2	0.3196	0	0.0001254
3	0.1394	0	0.07438
4	0.0742	0	609.34

The boundary conditions of the damper simulation are the same as those of the test. This simulation considered four displacement amplitude working conditions at 1.0 Hz for comparing test results and studies on subsequent stress and energy conversion. As shown in Figure 15, a fully fixed boundary condition was applied at the bottom end of the constrained steel plate. At the coupling point on the top surface of the shear steel plate, the displacement boundary condition was imposed, and a sinusoidal function condition was used with the loading controlled by displacement.

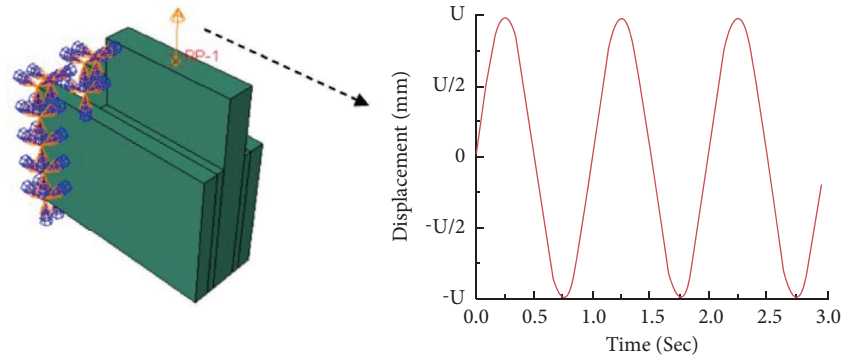

Figure 15: Boundary conditions of the damper.

5.4. Results and Discussion

5.4.1. Validation of Finite Element Simulation. A comparison of the finite element simulated hysteresis curves and the experimental hysteresis curves of the damper at 1.0 Hz frequency and displacement amplitudes of 1.2, 3, 6, and 9 mm is given in Figure 16. From the figure, it can be seen that the maximum damping force of the simulated curves at four displacements of 1.2, 3, 6, and 9 mm differs from the maximum damping force of the test results by 5.8%, 9.9%, 4.2%, and 6.9%, respectively, when compared with the test curves. The maximum viscous force of the simulated curves at four displacements differs from that of the test results by 10.8%, 5.5%, 9.4%, and 5.1%, respectively, and the hysteresis loop area of the simulated curves at four displacements differs from that of the test results by 10.7%, 11.3%, 13.6%, and 0.64%, respectively. It can be seen that the finite element simulation has less error compared with the experimental results and can be used for the numerical simulation analysis of right-angle viscoelastic dampers.

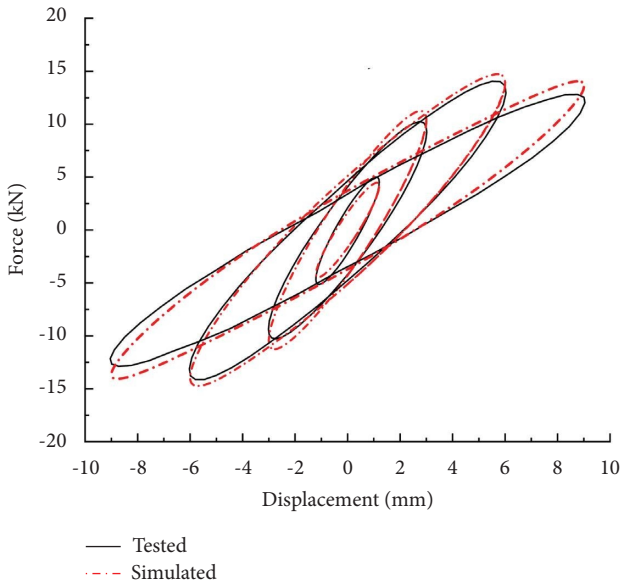

Figure 16: Comparison of simulation and test hysteretic curves.

5.4.2. Stress Analysis of Right-Angle Dampers. Figure 17 shows the stress distribution between the restraining steel plates and the viscoelastic layers for the maximum deformation of the viscoelastic layers at 1.2, 3, 6, and 9 mm displacement amplitudes. As can be seen from the figure, the stress on the steel plates is much larger than that on the viscoelastic layers. The stress distribution on the steel plates is approximately the same when the viscoelastic layers reach the maximum deformation at different displacement amplitudes, with the maximum stress at the corner point of the fixed end and radiating from the corner point of the fixed end (see the position of the circles in Figure 17(a)) to the far side. The lateral stress in the viscoelastic material layers is essentially equal, and there are areas of increased stress in the middle part of the material layers. On the top surface of the material layers, the stress increases in a parallel linear pattern from the part bonded to the restraining steel plate to the part bonded to the shear steel plate, the latter being the most stressed part of the entire viscoelastic layers. Comparing Figures 17(a)–17(d), it can be seen that with the increase of the displacement amplitude, the stress on the steel plates and viscoelastic layers gradually increases. The maximum stress on the steel plates and viscoelastic layers appears at 9 mm displacement amplitude, and the values are 56.3 and 2.2 MPa, respectively.

5.4.3. Analysis of Energy Dissipation of Right-Angle Dampers. Figure 18 shows the energy dissipation curves of the dampers for displacement amplitudes of 1.2, 3, 6, and 9 mm, and the time of work done by the external forces is all three seconds. The curves contain external work done (ALLWK), creep dissipation (ALLCD), strain energy (ALLSE), and plastic dissipation (ALLPD).

As shown in Figure 18(a), the work done by the external force at a displacement amplitude of 1.0 Hz frequency and a maximum displacement of 1.2 mm for the shear steel plate, i.e., the energy subjected to the damper, is 18.005 N-m, of which the energy dissipated by the viscoelastic material is 17.732 N-m, while the energy dissipated by the plasticity of the whole model is 0 N-m. It can be seen that the damper steel plate was not plastically deformed, and all the energy was basically dissipated by the viscoelastic material. As shown in Figure 18(b), the peak shear deformation of the

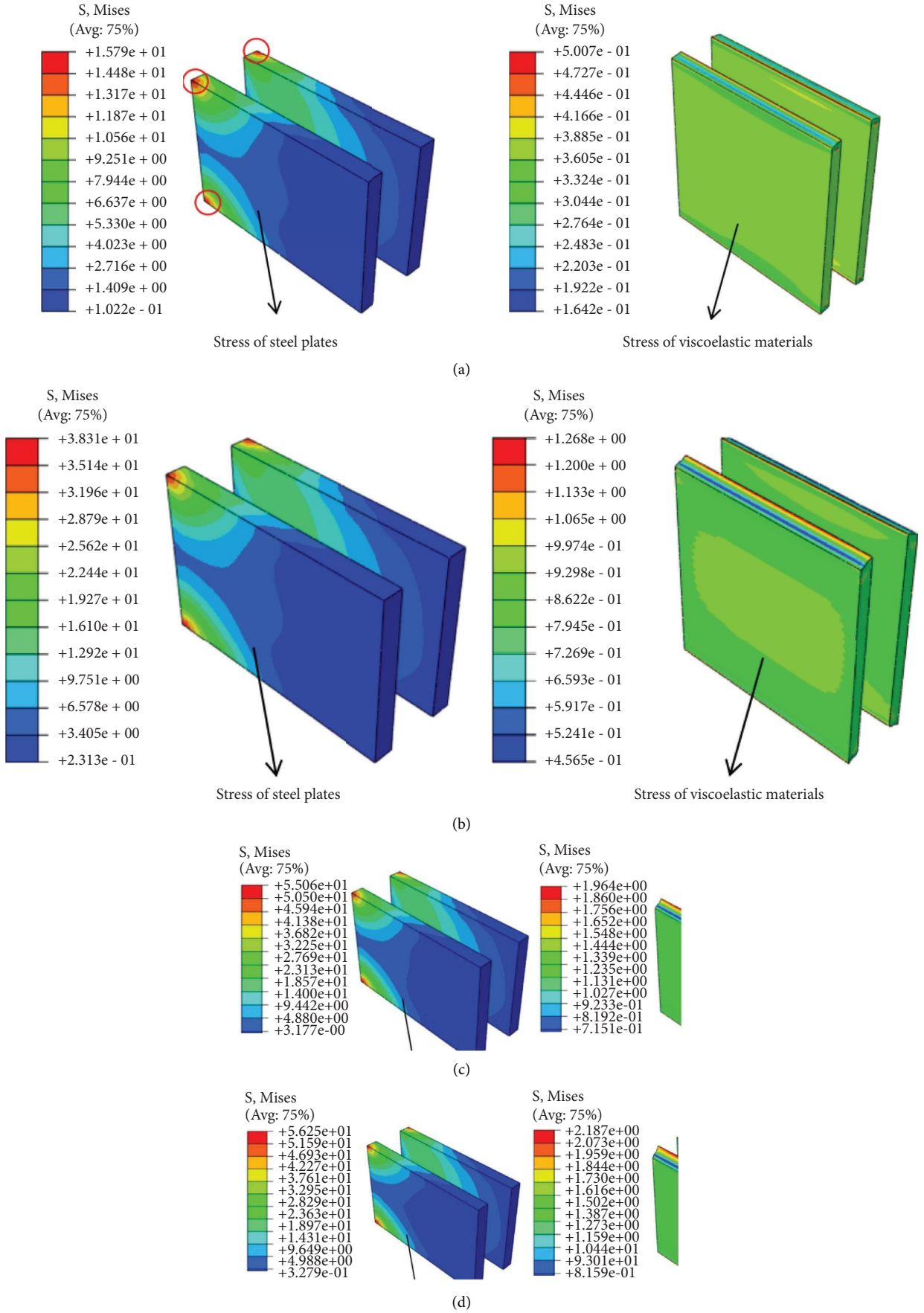

Figure 17: Stress nephogram of steel plates and viscoelastic materials at different displacements: (a) 1.2 mm; (b) 3 mm; (c) 6 mm; (d) 9 mm.

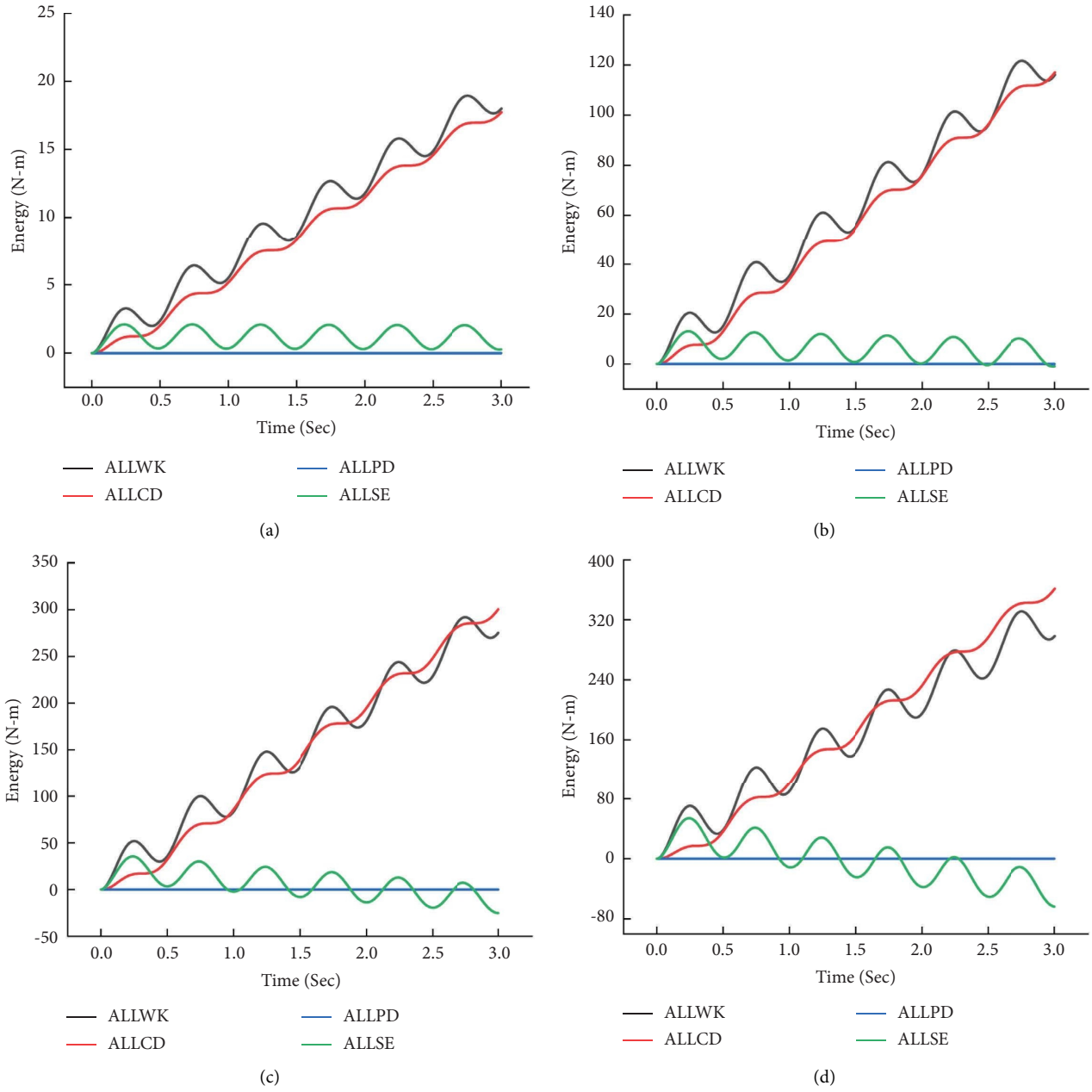

Figure 18: Energy dissipation curves at different displacements: (a) 1.2 mm; (b) 3 mm; (c) 6 mm; (d) 9 mm.

viscoelastic material of the damper is 3 mm, and the frequency is also 1.0 Hz. Under this condition, the input energy generated by the external work is 116.148 N-m, and the plastic dissipation energy is 0 N-m. The creep energy dissipation of viscoelasticity is 117.099 N-m, which is close to the work done by external forces, and all the energy was also dissipated by the viscoelastic material.

Figures 18(c) and 18(d) show the damper energy variation curves for the 6 mm and 9 mm displacement amplitude operating conditions at 1.0 Hz frequency, respectively. From the figure, it can be seen that the work done by the external force at two displacement amplitudes is 275.129 and 298.315 N-m respectively, and the plastic energy dissipation remains 0 N-m. The viscoelastic energy dissipation is 300.272 and 361.672 N-m for the two conditions, and the creep energy dissipation is higher than the work done by the external force. And at this time, the strain energy gradually becomes negative with the increase of external work time, and the energy is −25.197 and −63.598 N-m, respectively. At this point, the sum of the viscoelastic material energy dissipation and the negative strain is approximately equal to the work done by the external force. This may occur because the strain energy of the viscoelastic material was converted into heat energy and dissipated during the reciprocal shear motion, resulting in a negative situation. The work done by the external force is a fixed amount. In the simulation analysis of the damper as a whole, in order to maintain the energy conservation law of the object of study

(ALLWK = ALLCD + ALLSE + ALLPD), the energy consumption of creep will appear to exceed the work done by an external force.

The summary of energy dissipation in the numerical simulation is listed in Table 5, where U_{max} is the displacement amplitude. From Table 5, it can be seen that plastic energy dissipation did not occur throughout the loading at each displacement of the damper, implying that the steel plate of the right-angle damper did not participate in the energy dissipation. The plastic strain cloud of the damper at 9 mm displacement amplitude in Figure 19 shows that no plastic strain deformation occurred in all parts of the steel plate under the maximum stress loading condition, which again confirms the conclusion that there was no plastic energy dissipation in the damper. It can be seen that the dampers work well, but whether plastic dissipation occurs under large displacement loading conditions, or when large-size steel plates are used, needs to be studied further.

6. Control Performance Study of RVD

6.1. Overview of Steel Frame Model. In order to verify the damping effect of RVD on the steel frame, the structural response analysis of a single-span four-story scaled-down steel frame structure without control and with control (set up RVD damping system) was carried out in this paper by the method of establishing a refined three-dimensional model in ABAQUS, respectively. The material used for the steel frame is Q345 steel with a damping ratio of 0.05. The height and span of the frame are 1 m and 1.5 m, respectively. The frame beam is the I-beam section with a size of 100 mm × 68 mm × 4.5 mm × 7.6 mm, and the frame column is the box section with a size of 100 mm × 100 mm × 10 mm, as shown in Figure 20. The effect of placing 1660 kg and 700 kg mass blocks on floors 1 to 3 and floor 4, respectively, was achieved by increasing the density of frame beams. The dampers of the controlled structure were arranged at the top joints of the beams and columns in the Z-direction of the frame structure (as shown in Figure 21(a)). Figure 21(b) shows the numerical simulation model in ABAQUS. The size of the polyurethane material layer was 200 mm × 200 mm × 6 mm (length × width × thickness). The dimensions of the shear and restrained steel plates of RVD were set as 250 mm × 200 mm × 16 mm (length × width × thickness) and 250 mm × 200 mm × 12 mm (length × width × thickness), respectively. The loading seismic wave was selected as the EI Centro wave. The duration of the seismic wave was 30 s, and three kinds of peak accelerations (0.1 g, 0.2 g, and 0.4 g) were set for both uncontrolled and controlled structures.

6.2. Simulation Results and Analysis

6.2.1. Response of Structural Interstory Displacement. Comparative graphs of the interstory displacement response of the uncontrolled and controlled structures for the first floor under three different peak accelerations (0.1 g, 0.2 g, and 0.4 g) are given in Figures 22(a)–22(c). From Figure 22, it can be seen that the overall interstory displacement of the controlled frame is smaller than that of the uncontrolled frame during the whole seismic process, indicating that the PUE-type RVD can effectively reduce the interstory displacement of the frame structure during the entire seismic action.

Figure 23 gives the comparison of the maximum interstory displacement distribution curves along the height for each layer of the uncontrolled and controlled structures. Table 6 summarizes the maximum interstory displacement values of the uncontrolled and controlled frames and their damping rates, where the damping rate is the ratio of the difference between the maximum interstory displacement of the uncontrolled structure and the interstory displacement of the controlled structure to the maximum interstory displacement of the uncontrolled structure. As can be seen from Table 6, the damping effect of the maximum interstory displacement of the frame is obvious under different peak accelerations, and the damping rates of the displacement are roughly equivalent. Under the three peak accelerations, the damping rate is in the range of 42% to 43% for the first floor, about 45% for the second floor, and about 47% and 51% for the third and fourth floors, respectively. As the height increases, the damping effect also improves, and the fourth layer has the best damping effect. Under all working conditions, the maximum interstory displacement angle of the uncontrolled structure can reach 0.007 rad, which exceeds the code (0.004 rad). After setting the PUE-type RVD, the maximum interstory displacement angle is reduced to 0.0038 rad, which meets the code.

6.2.2. Response of Structural Acceleration. Figures 24(a)–24(c) show the comparison of the top-floor acceleration response between uncontrolled and controlled structures at three peak accelerations (0.1 g, 0.2 g, and 0.4 g), respectively. From the figure, the addition of RVD has a better effect on the acceleration control of the frame throughout the seismic process, while the maximum acceleration of the uncontrolled frame is reduced, indicating that the PUE-type RVD plays a positive role in limiting the acceleration of the frame.

Figure 25 gives the comparison of the maximum acceleration distribution curves along the height for each layer of the uncontrolled and controlled structures. Table 7 summarizes the maximum acceleration values of the uncontrolled and controlled frames and their damping rates, where the damping rate is the ratio of the difference between the maximum acceleration of the uncontrolled structure and the maximum acceleration of the controlled structure to the maximum acceleration of the uncontrolled structure. Combining the graph and table, it can be seen that the maximum acceleration value increases gradually as the number of layers increases, and the maximum value appears at the top layer for both uncontrolled and controlled structures. The range of damping rates from the first to the fourth layer under three earthquakes with different intensities is 3% to 11%, 29% to 33%, 24% to 26%, and 26% to 30%, respectively, and the second layer has the best effect for acceleration control under the overall comparison. Combining the acceleration response and displacement response, the PUE-type RVD has better control for displacement.

Table 5: Summary of energy dissipations obtained from numerical results.

U_{max} (mm)	Input energy (N-m)	Creep dissipation (N-m)	Strain energy (N-m)	Plastic dissipation (N-m)
1.2	18.005	17.732	0.273	0
3	116.148	117.099	−0.959	0
6	275.129	300.272	−25.197	0
9	298.315	361.672	−63.598	0

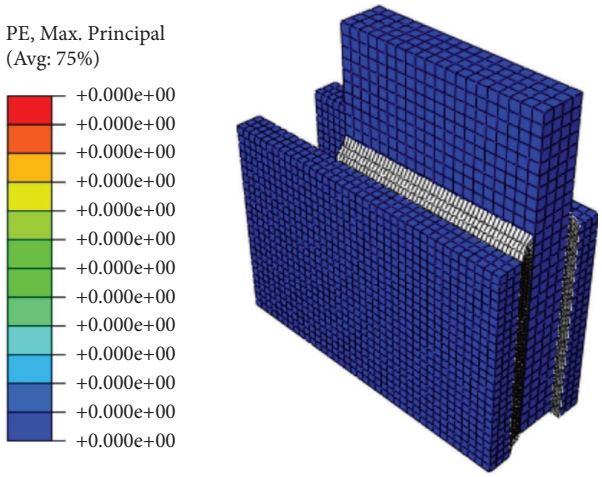

Figure 19: Plastic strain of RVD at the displacement of 9 mm.

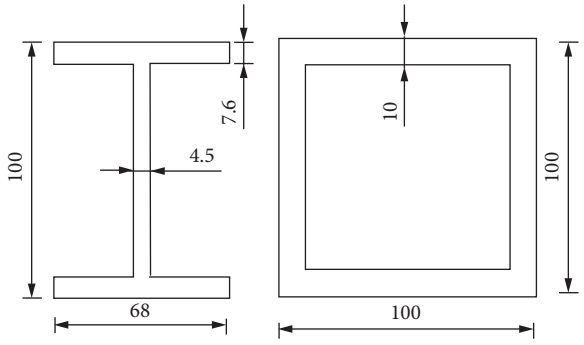

Figure 20: Sectional dimensions of beams and columns (unit:mm).

6.2.3. Response of Structural Interstory Shear Force. According to the acceleration time-history response curve obtained by the research model and combined with the mass distribution of the floor of the frame structure, the interstory shear force can be obtained through the following equation:

$$V_i(t) = \sum_{j=i}^{4} m_j a_j(t) (i = 1, 2, 3, 4), \quad (2)$$

where $V_i(t)$ is the shear force of the ith layer, m_j is the mass of the jth floor, and $a_j(t)$ is the relative acceleration of the jth layer.

Figure 26 gives the comparison of the maximum interstory shear force curves along the height for each layer of the uncontrolled and controlled structures. Table 8 summarizes the maximum interstory shear force values of the uncontrolled and controlled frames and their damping rates, where the damping rate is calculated in the same way as the displacement and acceleration. From the figure and table, it can be seen that the PUE-type RVD has a better control effect on the interstory shear force under all working conditions, and the damping rate reaches more than 30% under all working conditions. The interstory shear force decreases with the increase of height under the same working condition, and the maximum value appears at the first layer. Combining all the working conditions, it can be seen that RVD has the best control effect on the interstory shear force for the first and second layers compared with the other two layers.

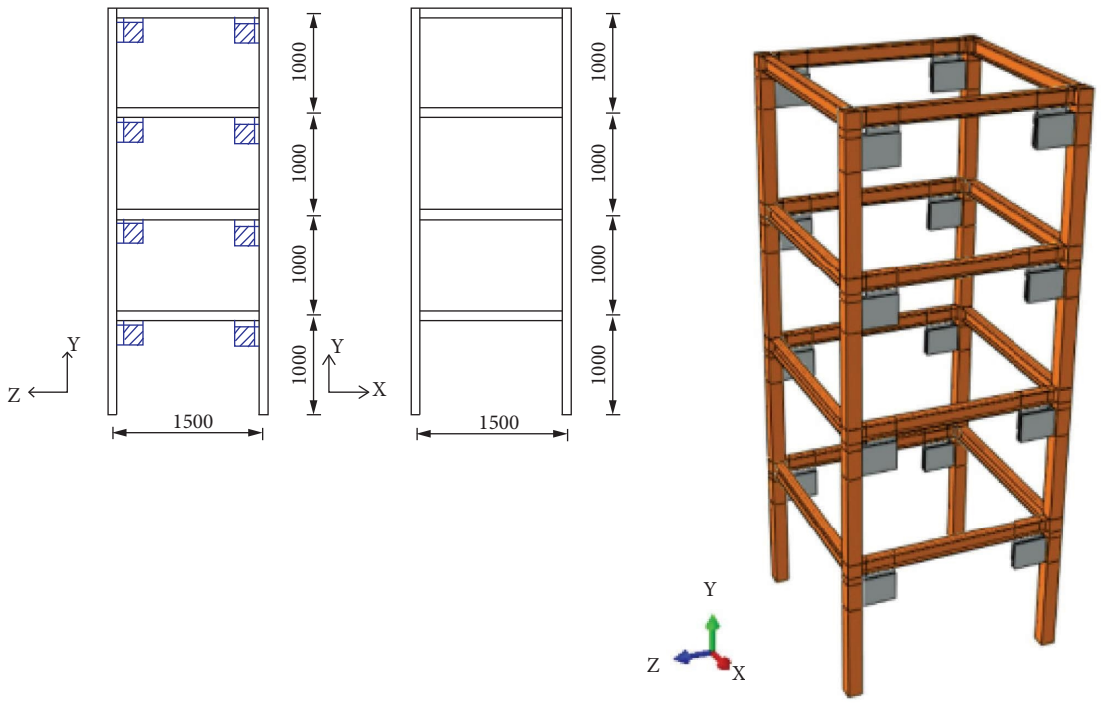

FIGURE 21: Schematic diagram of the frame structure with right-angle viscoelastic dampers: (a) frame structure and arrangement of dampers; (b) numerical simulation model in ABAQUS.

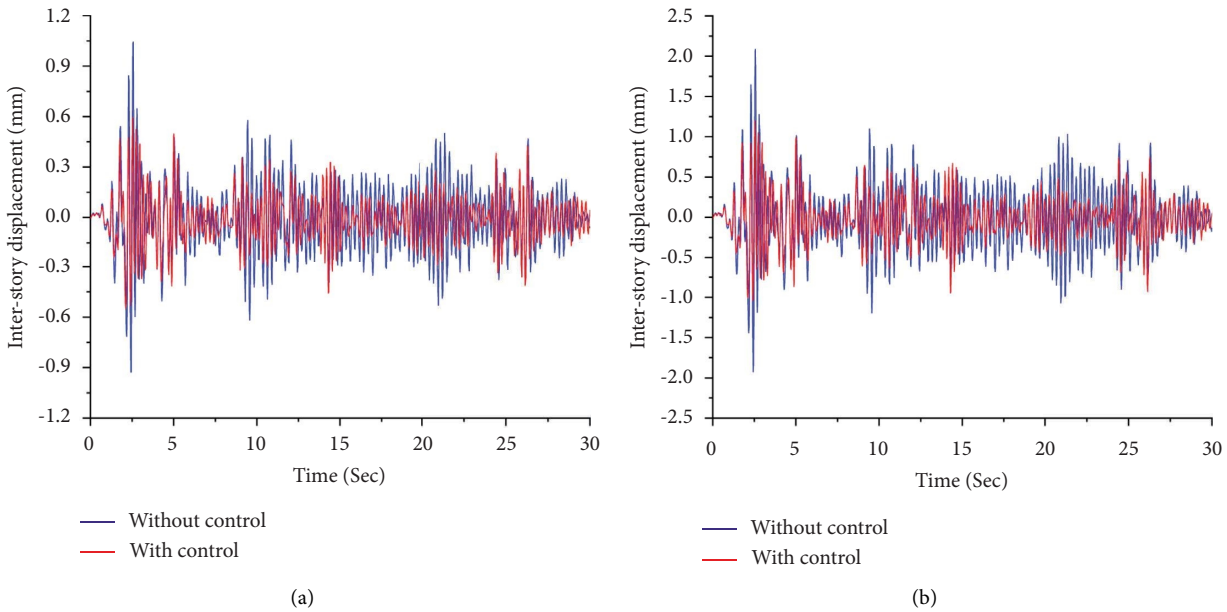

FIGURE 22: Continued.

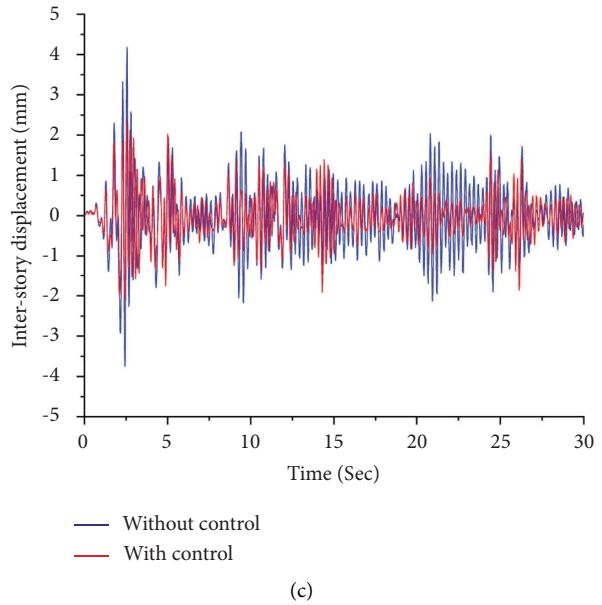

(c)

Figure 22: Time-history response of the interstory displacement for the first floor under different acceleration peaks: (a) 0.1 g; (b) 0.2 g; (c) 0.4 g.

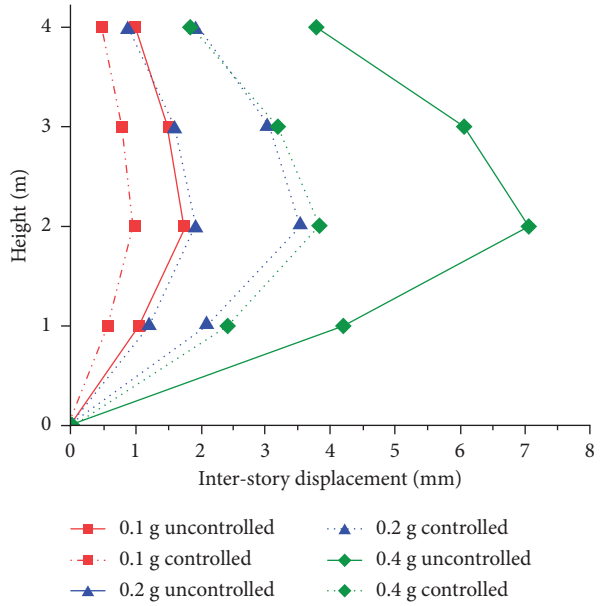

Figure 23: Curves of maximum interstory displacement along the height distribution for each layer of uncontrolled and controlled frames.

Table 6: Comparison of maximum interstory displacement for each layer between the frame without control and the frame with control.

Loading conditions			Maximum interstory displacement (mm)			
			First floor	Second floor	Third floor	Fourth floor
EI centro wave	0.1 g	Without control	1.04	1.76	1.52	0.96
		With control	0.59	0.96	0.80	0.47
		Damping rate (%)	43.27	45.45	47.37	51.04
	0.2 g	Without control	2.09	3.54	3.04	1.91
		With control	1.20	1.93	1.60	0.92
		Damping rate (%)	42.58	45.48	47.37	51.83
	0.4 g	Without control	4.18	7.08	6.07	3.80
		With control	2.40	3.85	3.19	1.85
		Damping rate/(%)	42.58	45.62	47.44	51.32

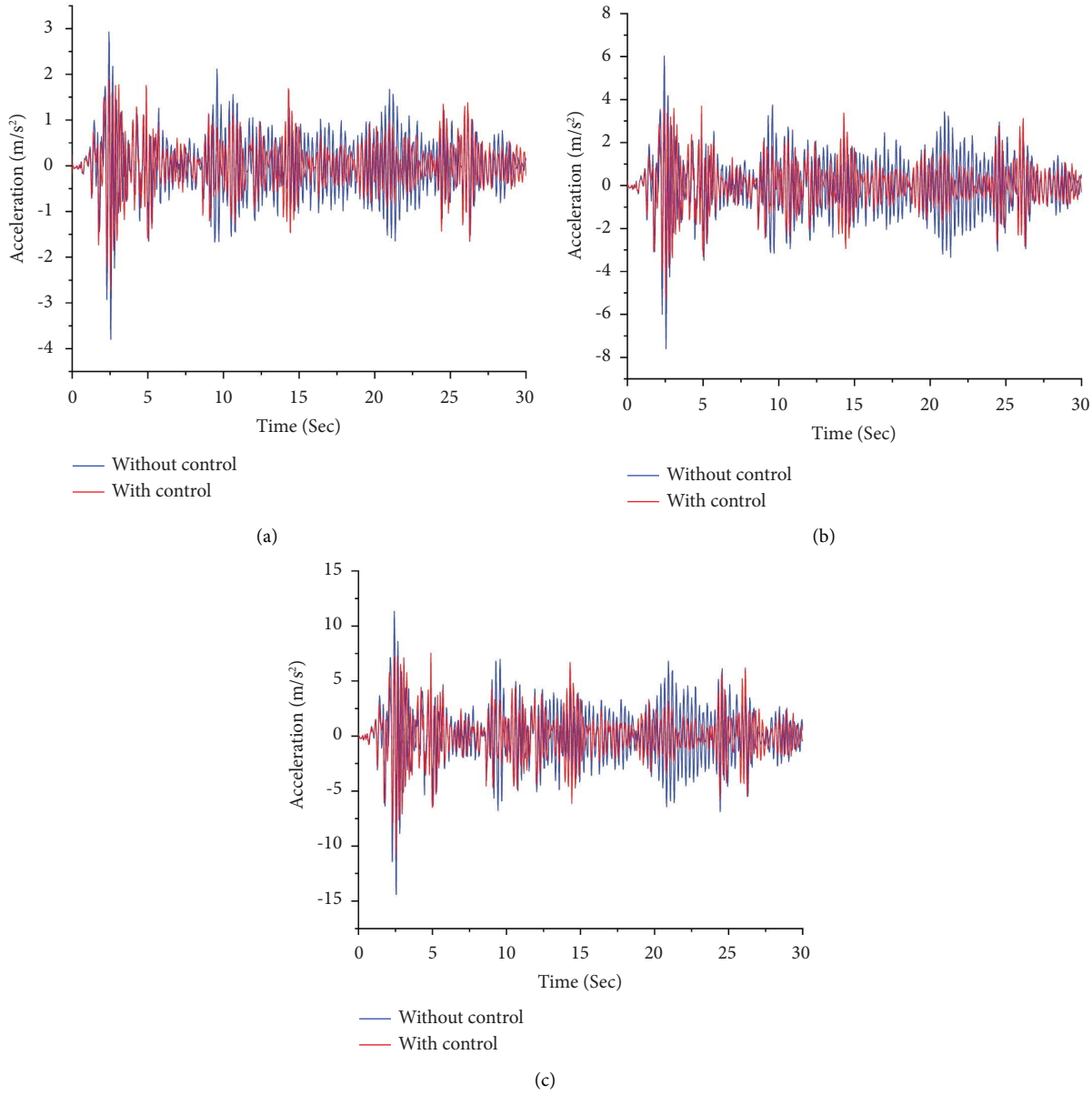

Figure 24: Time-history response of acceleration for the top story under different peak accelerations: (a) 0.1 g; (b) 0.2 g; (c) 0.4 g.

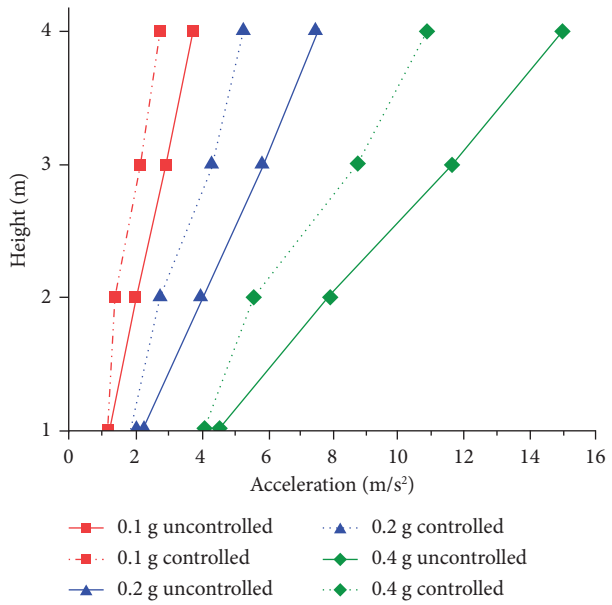

Figure 25: Curves of maximum acceleration along the height distribution for each layer of uncontrolled and controlled frames.

Table 7: Comparison of maximum acceleration for each layer between the frame without control and the frame with control.

Loading conditions			Maximum acceleration (m/s^2)			
			First floor	Second floor	Third floor	Fourth floor
EI centro wave	0.1 g	Without control	1.13	1.99	2.91	3.72
		With control	1.09	1.38	2.17	2.73
		Damping rate (%)	3.54	30.65	25.43	26.61
	0.2 g	Without control	2.26	3.98	5.82	7.45
		With control	2.03	2.70	4.33	5.28
		Damping rate (%)	10.18	32.16	25.60	29.13
	0.4 g	Without control	4.53	7.95	11.65	14.89
		With control	4.07	5.61	8.80	10.85
		Damping rate (%)	10.15	29.43	24.46	27.13

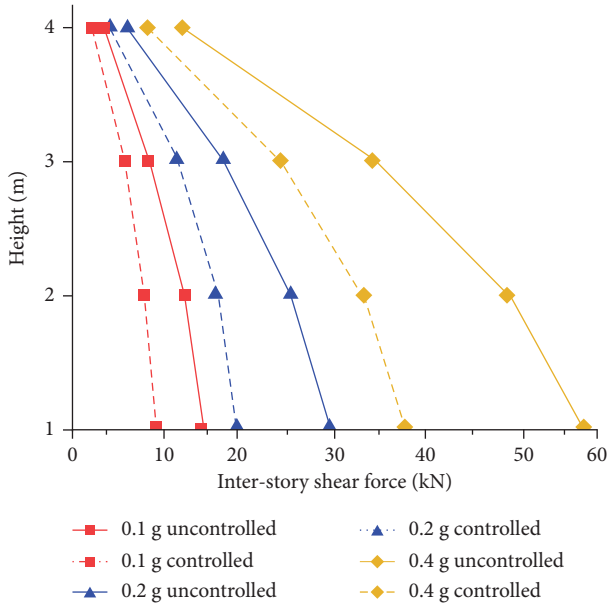

Figure 26: Curves of maximum interstory shear force along the height distribution for each layer of uncontrolled and controlled frames.

Table 8: Comparison of maximum interstory shear force for each layer between the frame without control and the frame with control.

Loading conditions			Maximum interstory shear force (kN)			
			First floor	Second floor	Third floor	Fourth floor
EI centro wave	0.1 g	Without control	14.20	12.10	8.31	3.02
		With control	9.21	7.84	5.67	2.04
		Damping rate (%)	35.14	35.21	31.77	32.45
	0.2 g	Without control	28.40	24.21	16.62	6.03
		With control	18.16	15.87	11.47	4.04
		Damping rate (%)	36.06	34.45	30.99	33.0
	0.4 g	Without control	56.79	48.42	33.23	12.06
		With control	36.6	32.2	22.91	8.15
		Damping rate (%)	35.55	33.50	31.06	32.42

7. Conclusions

This paper studied the dynamic thermodynamic properties of polyurethane damping materials and fabricated right-angle viscoelastic dampers using polyurethane as the energy-dissipating core material. Then, the dynamic characteristics of the damper were studied through the self-designed test loading device and scheme. Furthermore, the damper stress analysis and energy dissipation analysis were performed using finite element simulation. Finally, seismic time-history analysis was performed for uncontrolled and controlled (equipped with RVDs) steel frame structures. The designed dampers have good energy dissipation capacity and are suitable for seismic resistance of steel frame structures. The specific conclusions are as follows:

(1) The TA values of the polyurethane material and the loss factor of the polyurethane right-angle damper both peak at 2.0 Hz, which to a certain extent confirm the accuracy with each other. It is also shown that the polyurethane viscoelastic dampers made in this paper can give good play to the damping properties of viscoelastic damping materials.

(2) The right-angle damper has smooth and full hysteresis curves, with good energy dissipation capacity, and can be used for seismic resistance of assembled steel joints. The shape of the hysteresis loop varies with the displacement amplitude, and its hysteresis characteristics are of a nonlinear type. At all frequencies, the stiffness of the damper decreases with the increase of the displacement amplitude.

(3) The maximum damping force shows a trend of increasing and then decreasing with the increase of displacement amplitude, and the equivalent damping coefficient, storage modulus, loss modulus, and loss factor show a decreasing trend with the increase of the displacement amplitude. The equivalent damping coefficient at each displacement of the damper gradually decreases with the increase of frequency, while the frequency dependence of other dynamic parameters indexes is not obvious.

(4) The stress distribution of the viscoelastic material layer is basically symmetrical, and the extreme value of the stress appears on the connection line with the steel plate, and the steel plate for constraint appeared at the upper and lower end points of the fixed end. When the excitation level did not exceed 9 mm displacement amplitude, the energy was dissipated by the polyurethane at different excitation levels without plastic deformation of the steel plate. Under the maximum stress loading condition, the right-angle viscoelastic dampers never produced the plastic loss.

(5) The polyurethane right-angle damper has a good shock absorption effect under different earthquake actions. It has played a good role in limiting interstory displacement and acceleration and reducing interstory shear. The seismic-reduction rate of interstory displacement, acceleration, and interstory shear can reach 51%, 32%, and 36%, respectively. The results fully prove that polyurethane right-angle damper has significant energy dissipation capacity in steel structure joints.

Data Availability

Relevant data can be obtained by e-mail at xujunhong0321@126.com.

Conflicts of Interest

The authors declare that they have no conflicts of interest.

Acknowledgments

This work was supported by the Key Project of Large Multi-functional Vibration Table Array Laboratory of Beijing University of Architecture and Architecture (2022MFSTL02) and the National Natural Science Foundation of China (51978243).

References

[1] P. F. Zhang, M. Zhang, W. Zhang, G. H. Yao, S. M. Wu, and Y. Zhang, "Giant aneurysm of the left atrial appendage: detected by real-time 3-dimensional echocardiography," *Texas Heart Institute Journal*, vol. 37, no. 1, pp. 129-130, 2010.

[2] Y. L. Xu, *Wenchuan Earthquake Damage Investigation and Reflection on Safety of Building Structures*, China Architecture & Building Press, Beijing, China, 2009.

[3] L. W. Tong, Y. Z. Chen, Y. Y. Chen, and C. Fang, "Cyclic behaviour of beam-to-column joints with cast steel

connectors," *Journal of Constructional Steel Research*, vol. 116, pp. 114–130, 2016.

[4] B. G. Morgen and Y. C. Kurama, "Seismic design of friction-damped precast concrete frame structures," *Journal of Structural Engineering*, vol. 133, no. 11, pp. 1501–1511, 2007.

[5] B. G. Morgen and Y. C. Kurama, "Seismic response evaluation of posttensioned precast concrete frames with friction dampers," *Journal of Structural Engineering*, vol. 134, no. 1, pp. 132–145, 2008.

[6] A. Banisheikholeslami, F. Behnamfar, and M. Ghandil, "A beam-to-column connection with visco-elastic and hysteretic dampers for seismic damage control," *Journal of Constructional Steel Research*, vol. 117, pp. 185–195, 2016.

[7] Z. q Jiang, X. F. Yang, C. Dou, C. Li, and A. L. Zhang, "Cyclic testing of replaceable damper: earthquake-resilient prefabricated column-flange beam-column joint," *Engineering Structures*, vol. 183, pp. 922–936, 2019.

[8] S. H. Oh, Y. J. Kim, and H. S. Ryu, "Seismic performance of steel structures with slit dampers," *Engineering Structures*, vol. 31, no. 9, pp. 1997–2008, 2009.

[9] M. Latour, V. Piluso, and G. Rizzano, "Experimental analysis of beam-to-column joints equipped with sprayed aluminium friction dampers," *Journal of Constructional Steel Research*, vol. 146, pp. 33–48, 2018.

[10] T. Tani, S. Yoshitomi, M. Tsuji, and I. Takewaki, "High-performance control of wind-induced vibration of high-rise building via innovative high-hardness rubber damper," *The Structural Design of Tall and Special Buildings*, vol. 18, no. 7, pp. 705–728, 2009.

[11] H. Akehashi and I. Takewaki, "Modeling of resilience based on categorized recovery scenario and improving resilience with viscous damper," *Japan Architectural Review*, vol. 5, no. 3, pp. 279–294, 2022.

[12] H. Akehashi and I. Takewaki, "Resilience evaluation of elastic-plastic high-rise buildings under resonant long-duration ground motion," *Japan Architectural Review*, vol. 5, no. 4, pp. 373–385, 2022.

[13] C. X. Wu, Y. Zhou, X. Xu, C. Zhang, and X. S. Deng, "Experimental investigation on hysteretic performance of sector lead viscoelastic damper," *Journal of Building Structures*, vol. 35, no. 4, pp. 199–207, 2014.

[14] C. X. Wu, X. S. Deng, W. S. Lai, C. Y. Wu, and X. Xu, "Experimental comparison study on earthquake resistance performance of joint in amortization concrete frame with sector lead viscoelastic damper," *Earthquake resistant engineering and Retrofitting*, vol. 39, no. 5, pp. 81–87+123, 2017.

[15] C. X. Wu, D. B. Li, X. S. Deng, C. Yang, and X. Xu, "Experimental study on precast concrete moment-resisting frame system with sector lead viscoelastic dampers," *Structural Control and Health Monitoring*, vol. 28, no. 7, 2021.

[16] Y. J. Zhu, Y. Zhou, X. S. Deng, and C. X. Wu, "Analysis and design of frame structure with sector lead viscoelastic dampers," *Earthquake resistant engineering and Retrofitting*, vol. 36, no. 01, pp. 70–75, 2014.

[17] X. Xu, Y. Zhou, and C. X. Wu, "Finite element analysis and study on performance of sector lead viscoelastic damper," *Journal of Disaster Prevention and Mitigation Engineering*, vol. 32, no. 4, pp. 444–451+480, 2012.

[18] C. Zhang, W. Y. Huang, Y. Zhou, and W. L. Luo, "Experimental and numerical investigation on seismic performance of retrofitted RC frame with sector lead viscoelastic damper," *Journal of Building Engineering*, vol. 44, Article ID 103218, 2021.

[19] H. N. Li, X. Fu, Y. L. Li, and H. J. Liu, "Mechanical model and structural control performance of a new rotation-magnified viscoelastic damper," *Engineering Structures*, vol. 252, Article ID 113569, 2022.

[20] B. Y. Long, H. Zhang, and H. Y. Long, "A type of sector viscoelastic damper production mold," 2019.

[21] Q. Feng, M. L. Shen, J. M. Zhu, J. Li, J. Zhang, and S. Y. Guo, "Realization of polyurethane/epoxy interpenetrating polymer networks with a broad high-damping temperature range using β-cyclodextrins as chain extenders," *Materials & Design*, vol. 212, Article ID 110208, 2021.

[22] S. Praveen, J. Bahadur, R. Yadav et al., "Tunable viscoelastic and vibration damping properties of a segmented polyurethane synergistically reinforced with carbon black and anisotropic additives," *Applied Acoustics*, vol. 170, Article ID 107535, 2020.

[23] J. Xiaolin, X. Min, W. Minhui et al., "Preparation and molecular dynamics study of polyurethane damping elastomer containing dynamic disulfide bond and multiple hydrogen bond," *European Polymer Journal*, vol. 162, Article ID 110893, 2022.

[24] A. M. Castagna, A. Pangon, T. Choi, G. P. Dillon, and J. Runt, "The role of soft segment molecular weight on microphase separation and dynamics of bulk polymerized polyureas," *Macromolecules*, vol. 45, no. 20, pp. 8438–8444, 2012.

[25] T. Q. Yang, *Viscoelastic Mechanics*, Huazhong University of Science and Technology Press, Wuhan, China, 1990.

[26] Z. Shu, B. Ning, S. Li, Z. Li, Z. Gan, and Y. Xie, "Experimental and numerical investigations of replaceable moment-resisting viscoelastic damper for steel frames," *Journal of Constructional Steel Research*, vol. 170, Article ID 106100, 2020.